AIAA JOURNAL
Vol. 44, No. 6, June 2006

Skin-Friction Measurements on the NASA Hump Model

J. W. Naughton*
University of Wyoming, Laramie, Wyoming 82071
and
S. Viken† and D. Greenblatt‡
NASA Langley Research Center, Hampton, Virginia 23681-2199

The skin-friction distribution on a wall-mounted hump model has been obtained using oil-film interferometry. This effort is part of a larger study to provide validation cases for simulations of unsteady flows. The challenges of using oil-film interferometry on this model, including model curvature and close camera proximity, are discussed. Skin-friction measurements are obtained over most of the hump model, including especially high-quality measurements in the separated and reattachment regions. These results highlight the method's ability to capture a wide range of skin friction including measurements in reverse-flow and high-gradient regions. The wall skin-friction data are shown to complement other experimental data, and the use of independent skin-friction measurements for scaling in wall-bounded flows is emphasized. A comparison with results from several computational simulations of the same flow is presented. The comparison indicates that, for the most part, the computations accurately predict the skin-friction ahead of separation, but fail to predict the reattachment point correctly, and thus the comparison in the separated and recovery regions of the flow is poor. The ability of the skin-friction measurements to pinpoint regions where the computation performs poorly in the near-wall region is also presented. From these results, it is evident that independent skin-friction measurements should be a part of all validation experiments conducted in wall-bounded flows.

Nomenclature

C_f	=	skin-friction coefficient
C_p	=	pressure coefficient
c	=	model chord
h	=	oil height
i	=	pixel intensity
i, j	=	image location in pixels
M	=	Mach number
n	=	surface normal; surface streamline divergence
n_a	=	air index of refraction
n_f	=	oil index of refraction
P	=	static pressure
q	=	dynamic pressure
Re	=	Reynolds number
$S_{i,i}$	=	autospectrum of intensities
t	=	time
U_∞	=	freestream velocity
u	=	mean streamwise velocity
u_τ	=	friction velocity
$\langle u'u' \rangle$	=	normal Reynolds stress
u^+	=	nondimensional velocity (viscous scaling)
X, Y, Z	=	model coordinate system for photogrammetry
X_c, Y_c, Z_c	=	perspective center
x, y	=	image coordinate system
x, y, z	=	streamwise, vertical, and cross-stream coordinates
y^+	=	nondimensional distance from the wall (viscous scaling)
δ	=	boundary-layer thickness
θ	=	view angle with respect to surface normal
θ_i	=	incidence angle
λ	=	wavelength
μ	=	dynamic viscosity
ν	=	kinematic viscosity
$\rho_{i,\text{if}}$	=	cross-correlation coefficient
τ, τ_w	=	wall shear stress
ϕ	=	phase angle

Subscripts

a, b	=	locations a and b
c	=	chord
i	=	iteration
max	=	maximum
θ	=	based on momentum thickness
1, 2	=	conditions at times 1 and 2
∞	=	freestream

Presented as Paper 2004-2607 at the AIAA 24th Aerodynamic Measurement Technology Conference, Portland, OR, 26 June–1 July 2004; received 5 November 2004; revision received 23 June 2005; accepted for publication 8 July 2005.

*Associate Professor, University of Wyoming Aeronautical Laboratories, Department of Mechanical Engineering, Dept. 3295, 1000 E. University Avenue. Associate Fellow AIAA.

†Aerospace Engineer, Mail Stop 170, Flow Physics and Control Branch. Member AIAA.

‡National Research Council Research Associate, Mail Stop 170, Flow Physics and Control Branch. Senior Member AIAA.

I. Introduction

IN conjunction with several agencies and researchers, NASA Langley Research Center has undertaken an effort to evaluate the ability of computational models to predict unsteady flowfields typical of flowfields desired to be controlled using active flow control strategies. One of the suite of test cases being used in this effort is a two-dimensional, wall-mounted Glauert–Goldschmied-type body (a wall-mounted hump) that has a geometry similar to that studied by Seifert and Pack.[1] Surface and flowfield measurements have been obtained on this body to provide data with which the computational results can be validated. In its baseline configuration, this model provides a low-speed test case with separation and reattachment. The model can also be operated with steady suction and zero-mass efflux jets. High-quality measurements have been taken on this model including surface flow visualization, steady and unsteady pressure measurements, and particle-image velocimetry (PIV) measurements

of the flowfield. Details of these measurements can be found in Greenblatt et al.[2]

To provide both quantitative and qualitative information to assess the near-wall performance of the computational simulations, wall shear-stress data have been acquired on the baseline configuration. Shear-stress measurements are often much more sensitive to the boundary-layer state than pressure measurements[3] because shear stress is dependent on the near-wall velocity profile. When coupled with surface-pressure and flowfield measurements, shear-stress measurements provide additional valuable information to evaluate computational results. Shear-stress measurements in flows such as that over the hump model with varying shear stress, pressure gradients, separation, and reattachment are particularly difficult. In such complicated cases, many traditional shear-stress measurement techniques fail or produce results with large uncertainty. However, oil-film interferometry, a technique that relates the local thinning of an oil film to shear stress, is capable of accurate measurements in such flows.

The paper discusses the use of oil-film interferometry for skin-friction measurements on the wall-mounted hump. The objectives of this work were to obtain high-quality skin-friction measurements on the hump model's complex geometry and to use these measurements to aid in the assessment of computational simulations. To obtain the skin-friction measurements on the hump model, special considerations were taken in acquiring and analyzing the interferograms obtained in this study. The resulting skin-friction measurements revealed that accurate measurements could be obtained in such flows and that such measurements provided additional insight that helped both to understand the flow physics and to assess computational simulations.

II. Experimental Setup

The shear-stress measurements were carried out on a wall-mounted hump located nearly 2 m from the leading edge of a splitter plate. A schematic of the hump with important dimensions is shown in Fig. 1. The forward curved ramp terminated with a slot just downstream of the maximum height location. Another curved ramp on the aft of the body made a smooth transition back to a rear splitter plate. Vertically mounted end plates were used to promote two-dimensionality. A flap at the rear of the aft splitter plate was adjusted to keep the flow attached on the leading edge of the forward splitter plate. This model was mounted in a wind tunnel with a 0.771×0.508 m cross section. With the model installed, the distance from the splitter plate surface to the ceiling was 0.382 m. The flow was tripped near the leading edge of the splitter plate such that the boundary layer was measured to be turbulent at 2.14 chord lengths upstream of the hump model. The boundary-layer thickness at this upstream location was 30.5 mm.

To describe the flowfield on the surface of this body, flow visualization in the form of oil-film interferograms shown in Fig. 2 will be used. Although the oil-film technique has not been discussed at this point, the unprocessed images are useful because they provide an indication of the surface flow. In addition, the viscosity of the oil used to produce these interferograms varied, and they were exposed to the flow for different periods of time; regions of higher shear

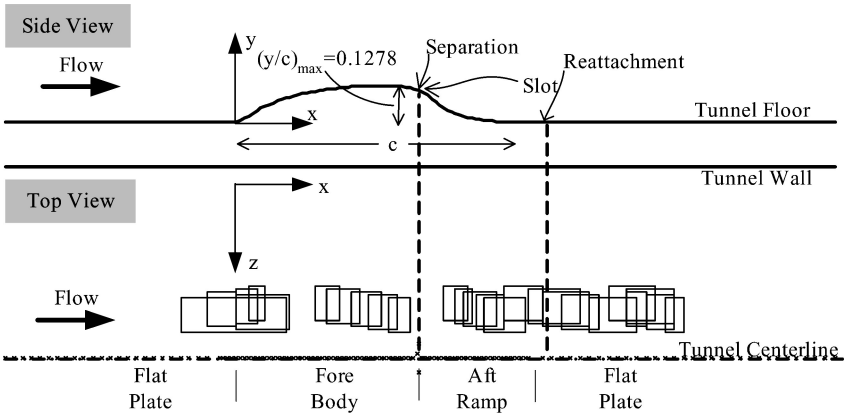

Fig. 1 Side and top views of the hump model showing the location of the interferograms obtained. The coordinate system used in this test and important model and flowfield features are also shown.

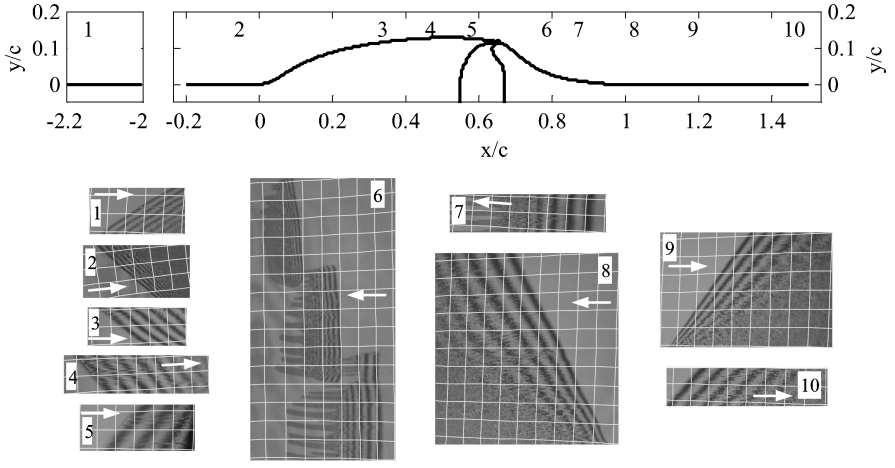

Fig. 2 Side view of the hump model with interferograms from different locations shown. The approximate locations of the middle of the interferograms are shown in the side view. The fringe spacing is dependent on the local wall shear stress τ_w, the time t the oil is exposed to the flow, and the oil viscosity ν: 1) $t = 524$ s, $\nu = 50$ cS; 2) $t = 660$ s, $\nu = 50$ cS; 3) $t = 615$ s, $\nu = 100$ cS; 4) $t = 652$ s, $\nu = 100$ cS; 5) $t = 614$ s, $\nu = 100$ cS; 6) $t = 1226$ s, $\nu = 20$ cS; 7) $t = 817$ s, $\nu = 20$ cS; 8) $t = 800$ s, $\nu = 20$ cS; 9) $t = 790$ s, $\nu = 20$ cS; and 10) $t = 508$ s, $\nu = 20$ cS. The grid overlaid on the images is 6.35 mm square, and the images have been scaled so that the areas represented by the grid squares are approximately constant.

stress will exhibit widely spaced fringes, whereas lower shear stress is indicated by closely spaced fringes. In many cases, oil has often been applied to the surface in a slanted line (not at a constant x location) to make gradients in the shear stress easier to see. The top of Fig. 2 shows a side view of the model with numbers indicating the approximate center of each of the 10 interferograms shown in the lower part of the figure. Each of these images has been scaled so that the area shown by each image is roughly proportional to the planform area (projection on the $x - z$ plane) it occupies. This scaling is demonstrated by the faint white grid shown in the figures that indicates lines of constant x and z spaced 6.35 mm apart. For each of the interferograms shown, the viscosity and time of exposure are provided in the figure caption. An arrow that indicates the direction of the local surface flow to distinguish between regions of forward and reversed flow on the model surface is also included in each figure.

The flow on this model starts well upstream of the hump where a turbulent boundary layer forms on the splitter plate. Interferogram 1 that was obtained in this upstream region can thus be used as reference for all of the other images. As the boundary layer approaches the model, the flow on the surface decelerates and nearly separates as indicated by the closer fringe spacing in interferogram 2 that used the same viscosity oil as interferogram 1 and was exposed to the flow for a longer time. The flow then accelerates over the forward part of the hump producing an area of very high shear as indicated by the increased fringe spacing in interferograms 3, 4, and 5. Note that, not only are the fringes spaced further apart, the oil viscosity is also double that of the oil in interferogram 1. The flow then separates near the slot, and a region of reverse flow exists on the model surface as is evident in the direction of oil flow in interferograms 6–8. At some locations in this reverse-flow region, the shear stress is very low (interferogams 6 and 8), whereas in the middle of the region it actually becomes significant (interferogram 7). In these three cases, the oil viscosity is only 40% of that used in interferogram 1. The shear is very low in interferogram 6 as indicated by both the tight fringe spacing and the long exposure time that is nearly two-and-one-half times that used to produce interferogram 1. Near reattachment, the gradients in both directions (toward and away from separation) are high as indicated by the increasing fringe spacing from bottom to top in interferograms 8 and 9. Again note the lower viscosity oil used to obtain these images and their nearly identical exposure time (one-and-one-half times that used for interferogram 1) suggesting that the shear stress in this region is quite low. Interferogram 10 in the region downstream of separation indicates the increasing wall shear stress in the recovery region.

As evident in Fig. 2, oil-film interferometry measurements of skin friction have been obtained along much of the hump model surface. Figure 1 shows a plan view of the model with all of the measurement locations highlighted (with the exception of the measurement taken far upstream). Of the images obtained, 25 have been processed and have yielded more than 2700 individual skin-friction measurements. All of the interferograms have been acquired at a single flow condition, $Re_c = 9.29 \times 10^5$ and $M_\infty = 0.100$, which is close to the so-called computational fluid dynamics (CFD) test case ($Re_c = 9.36 \times 10^5$).

III. Oil-Film Interferometry

The oil-film interferometry method used here is an outgrowth of much previous work on this technique. Originally proposed by Tanner and Blows[4] based on the oil-film equations developed by Squire,[5] the method has undergone much development, notably by Monson et al.,[6] Zilliac,[7] Garrison and Ackman,[8] and Naughton and Brown[9] among others. The method has also evolved from a small laboratory instrument to one that has been used in large wind tunnels as discussed by Driver.[10] The oil films used in this method typically have height to length ratios of 10,000–100,000 ensuring that they are essentially nonintrusive. Although the films change very slowly, they essentially respond instantaneously to changes in shear stress ensuring that the measurement yields the true average of the wall shear stress. For further information about the technique, see Naughton and Sheplak[11] for an overview and Brown and Naughton[12] for a detailed treatment of the equations. In comparison to other shear-stress measurement techniques, oil-film intereferometry is relatively easy to implement, inexpensive to implement (with the exception of a good camera), and, if performed properly, can produce very accurate results.

A. Theory and Implementation

Oil-film interferometry is effective because of the motion of an oil subjected to an external shear force, which is governed by the thin-oil-film equation[12]

$$\frac{\partial h}{\partial t} + \frac{\partial}{\partial x}\left(\frac{\tau_{w,x} h^2}{2\mu}\right) + \frac{\partial}{\partial z}\left(\frac{\tau_{w,z} h^2}{2\mu}\right) = 0 \tag{1}$$

Here, the pressure gradient, gravity, and surface-tension terms have been neglected because the wall shear-stress term dominates when the oil thickness becomes small (on the order of microns typically). As indicated by this equation, when a shear is applied to the oil film, its height will change with time. If the oil height can be measured at one or more times and the local flow angle is known, the shear stress can be determined using

$$C_{f,i+1}^{\frac{1}{2}} = \frac{\int_0^x (n/C_{f,i})^{\frac{1}{2}}\,\mathrm{d}x}{h\sqrt{n}\int_0^t (q/\mu)\,\mathrm{d}t} \tag{2}$$

which is a modified form of the equation proposed by Garrison and Ackman.[8] This iterative solution requires an initial guess that is provided by the constant shear-stress solution

$$C_{f,1} = \frac{\mu x}{qht} \tag{3}$$

From Eq. (2) it is clear that the streamline divergence n and the integral quantity $\int_0^t (q/\mu)\,\mathrm{d}t$ are required before a solution can be obtained. The integral is determined by monitoring the dynamic pressure during the test and by knowing the oil viscosity. The viscosity is often the largest source of error in this technique,[7] and so its value must be precisely known. For this test, the plate temperature has been monitored during testing, and the oil has been calibrated as a function of temperature. The streamline divergence n for this test is simply set to unity because there is no streamline divergence or convergence in this two-dimensional flow. A positive aspect of Eq. (2) is that it can capture shear-stress gradients that occur over the region covered by a single interferogram. This feature is crucial in the current test.

The use of interferometry for the measurement of the oil height was first proposed by Tanner and Blows.[4] As shown in Fig. 3, monochromatic light striking the oil from above is partially reflected and partially transmitted. The transmitted portion of the light reflects from the surface and exits the oil with a phase difference from the beam that was originally reflected. When these beams are focused by a lens onto an image plane, they constructively or destructively interfere. The type of interferometry that uses a single beam that is divided by some interface is known as amplitude splitting or Fizeau interferometry. By illuminating the entire oil film, an interference pattern such as that shown at the top of Fig. 3 is formed. The oil height distribution at some time t_1 changes to a new height distribution at a later time t_2 because of the shear acting on the oil film. The

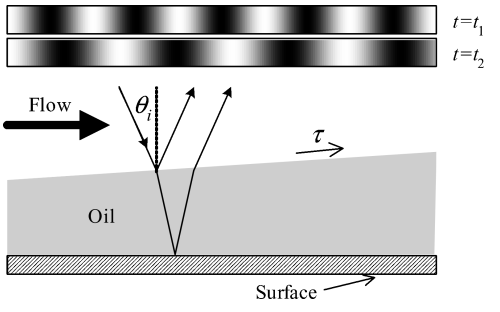

Fig. 3 Interference process in oil-film interferometry.

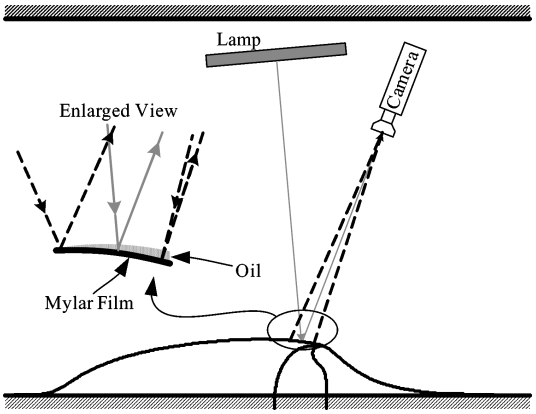

Fig. 4 Schematic of the oil-film interferometry arrangement in the wind tunnel.

interference pattern can be thought of as either indicating contours of constant oil height or phase difference between the reflected and transmitted beams. If the phase difference can be determined, then the oil height distribution can be calculated using

$$h = (\lambda\phi/4\pi)\left(1\Big/\sqrt{n_f^2 - n_a^2 \sin^2\theta_i}\right) \tag{4}$$

A discussion of the determination of the phase is presented in Sec. III.B.

The optical arrangement used to measure the interferometry in this test is quite simple and is shown in Fig. 4. Mylar film (Monokote Industries) was applied to the model to provide an appropriately reflective surface. A monochromatic light source (Edmunds Scientific) illuminated the Dow Corning 200 fluid used for the oil in this test. The reflected light was imaged using a Nikon D1X digital camera with a resolution of 3008×1960 pixels and a variable focal length lens. The camera and light source were mounted on a traverse such that they could be moved into the test section prior to and after a test. The lamp and camera had to enter the test section because there was insufficient optical access from the top of the test section. The close proximity of the camera to the test model (on the order of 25 cm) presented a challenge for processing the images. In addition to creating enhanced perspective effects, the incidence angle of the reflected light varied from point to point as shown in the close-up in Fig. 4. In addition, the close proximity and need to precisely move the camera to a specific location precluded obtaining more than one interferogram during a single test. A typical area of the model imaged by the camera was 100×75 mm.

During a typical test, the following procedure was used to obtain interferograms. The camera and light source were traversed into the test section, and the imaging region was determined. A picture containing a reference grid was then obtained. The camera and light source were removed from the tunnel, and oil was applied to the model in the region to be imaged. The oil was applied as thin lines if a continuous film were to be imaged and as dots if oil streaks were of interest. The oil viscosity used varied from 20 cS in the low shear locations to 100 cS in the highest shear regions. After applying the oil, the tunnel was closed and was operated at the desired conditions for 6–10 min depending on the local shear and oil viscosity. During this time, the temperature of the model and the dynamic pressure were monitored. The tunnel was then stopped, and the camera and light source were traversed into the tunnel where an interferogram image was obtained. An example interferogram acquired as part of this test is shown in Fig. 5. In this figure, pressure taps used to help identify the location of the image and a line indicating the approximate line along which the oil was applied are shown. The oil was applied as a slanted line for most interferograms obtained in this study to take advantage of the two dimensionality of the flow to obtain multiple redundant measurements. The length of time that the tunnel was run varied such that the fringe spacing was sufficient for analysis (those shown in the figure are typical of an adequate fringe spacing) and the on-condition time was long relative to startup and shutdown times. The results presented here were obtained from images such as that in Fig. 5 taken primarily over a three-day period.

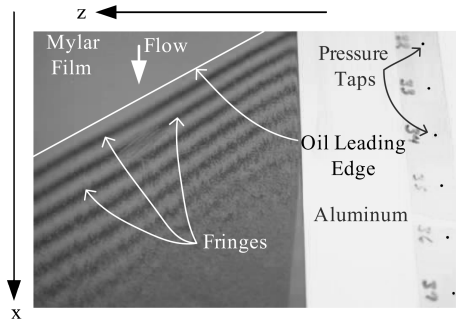

Fig. 5 Typical interferogram obtained using oil-film interferometry.

There were several challenges that were posed by this test that required a modification of the typical interferogram analysis used by the authors. As is evident in Fig. 4, the close proximity of the camera and the high degree of curvature at certain locations on the model ensured that the incidence angle viewed by each pixel in the camera would vary substantially across even the small distances imaged by the camera. This was important because the oil height determined from the phase using Eq. (4) is dependent on the local value θ_i. High spatial shear-stress gradients also required that a method that could handle shear-stress gradients, such as that provided by Eq. (2), be used. In addition, because the results were to be used for CFD validation, good accuracy in both space and skin-friction values was desired. The processing steps required to address all of these challenges are discussed next.

B. Image Analysis

The method used to analyze the interferograms acquired in this test is similar to that the authors have used in the past.[13,14] As already suggested, some modifications to the standard analysis have been necessary for this test. A brief overview of the steps used to analyze the data will be given first followed by a description of the special considerations necessary for the current test.

The first step in analyzing the interferograms is to identify points in the image that correspond to known physical locations on the model. This registering of the image is important so that a mapping from object space into image space can be accomplished. In the past, simple mapping methods have been used, but, because of the special requirements of this test, photogrammetry has been used for this purpose. Once the relationship between image space and object space is known, lines along the flow direction are extracted from the image. For the current test, the flow is two dimensional, so that lines along the model at constant z are selected. The intensity pattern extracted from the interferogram looks like a cosine wave. The peaks and valleys of this wave that represent the maximas and minimas of the interference are identified using the Fourier-transform/correlation approach described by Decker et al.[15] In this approach, the dominant frequency in the interferogram is determined using a Fourier transform, and then a cosine wave with the same frequency is correlated with the original intensities. The result is a cleaner signal with clear peaks and valleys. The locations of the peaks/valleys are determined using simple search criteria, and the phase is determined at those points. Knowing the phase, the local incidence angle, and the illumination wavelength, the oil height is determined using Eq. (4). The height information is used along with the integral value $\int_0^t (q/\mu)\,\mathrm{d}t$ to determine the skin friction using Eq. (2).

The new challenge posed by this test is the appropriate registration of images taken on this curved model at close proximity. Here, photogrammetry is used to relate camera and object space. Photogrammetry methods applied to wind-tunnel testing are described in detail in Cattafesta and Moore[16] and Liu et al.[17] Figure 6 shows the importance of using photogrammetry for oil-film interferometry. First, a mapping of image space (x, y) to physical space (X, Y, Z) is required so that the fringe spacing can be determined in physical

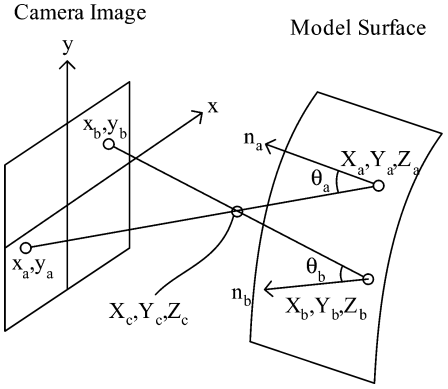

Fig. 6 Image (x, y) object (X, Y, Z) coordinate pairs indicating the effect of both perspective and model curvature on the observation angle θ. The perspective center (X_c, Y_c, Z_c) and local surface normals n are also shown.

units (meters or millimeters in this case). This information is required in addition to the oil-film height so that Eq. (2) can be solved. Second, the angle θ between the observation direction and the local surface normal is required to calculate the oil height because, for specular reflection, the incidence angle θ_i is equal to θ. This additional spatial information requirement is perhaps unique to oil-film interferometry. As is evident in Fig. 6, this angle can vary quite substantially across the image. To determine the spatial mapping and local incidence angle, the properties of the camera/lens systems (the interior orientation parameters), the location of the perspective center (X_c, Y_c, Z_c) and the orientation angles (the Euler angles) of the camera (collectively known as the exterior orientation parameters), and the location of several reference points on the model all need to be known.

In the current test, the model geometry is known precisely such that the location of reference points in the image can be determined. Using these points and the approximate values for the camera/lens system, the perspective center and the orientation angles are determined using an optimization method (Liu, T., personal communication, June 2004). With these values, the angle θ and image location x, y can be determined for each model location X, Y, Z specified. Higher accuracy in the angle θ could have been obtained if a camera calibration had been carried out to determine more precise values for the properties of the camera/lens system. Fortunately, θ is not very sensitive to these properties, and the effect on the calculated skin-friction values has been determined.

The analysis discussed here has been implemented in the MATLAB® language using a suite of routines that has been developed specifically for analyzing interferograms obtained using oil-film interferometry.[14] These routines have been assembled into an analysis program that takes advantage of the two-dimensional flow in the present test.

1. Uncertainty

A full uncertainty analysis for each of the skin-friction values determined in this study was carried out considering many of the uncertainties discussed by Zilliac[7] and Naughton and Brown.[18] Of the uncertainties considered, several biases were found to have a dominant effect including the oil viscosity, photogrammetry inaccuracies, and precision uncertainties. The uncertainty in the viscosity arose from both its calibration and knowledge of the temperature of the oil. Both of these effects were considered. The uncertainty caused by the photogrammetry was also considered, but it was found to be, in most cases, significantly less than the other uncertainties. Also included was the "precision" uncertainty that was calculated by averaging across the model in z and over small, but finite, regions in x. A typical number of averages assigned to any one location was 25. This precision uncertainty included variations in the results caused by electronic noise, varying fringe visibility, artifacts in the fringe pattern as a result of dust, and Mylar surface imperfections among other possible contributors. In addition, this uncertainty included any variations that appeared as a result of a departure from two dimensionality (of which little was observed). Because each of these uncertainties was considered to be independent, the total uncertainty was determined by summation in the rms sense.

An uncertainty that was not possible to evaluate in this study was the startup and shutdown effects that were present since the interferograms were taken after the run. Although these effects add uncertainty, they were minimized by casting the solution in terms of the skin-friction coefficient, which is expected to vary less than the wall shear stress itself, and ensuring that the tunnel was "on-condition" an order of magnitude longer than the time associated with startup and shutdown.

Another source of concern in this study was the measurement of shear stress near separation and attachment where the wall shear stress drops to zero. At separation and attachment, the pressure gradient and gravity terms neglected in Eq. (1) become important. However, these terms are multiplied by h^3 rather than the h^2, which multiplies the wall shear-stress term, thus indicating that these terms become insignificant as soon as the shear stress becomes nonzero. Here, measurements were avoided near attachment for the practical reason that the oil simply took too long to develop.

2. Example Analysis

To demonstrate the analysis process, the result of analyzing the interferogram shown in Fig. 7 is discussed here. The locations of the pressure taps (circles in the figure) and reference points (crosses in the figure) are first identified in the image so that photogrammetry can be used as just discussed. Using the results from the photogrammetry analysis, lines of constant x and z have been drawn in Fig. 7, where the perspective effect is clearly observed. Next, several parallel lines are extracted from the image along lines of constant z. The average intensity from several such lines near the white dotted line in Fig. 7 is shown in Fig. 8a with the mean removed. A portion of the autospectrum of the intensity is shown in Fig. 9, where a dominant frequency away from zero frequency (corresponding to the frequency whose amplitude has a symbol at the peak) corresponding to the quasi-sinusoidal intensity is quite evident. The broadening of this peak indicates that there is some variation in the frequency of the periodicity of the intensity signal in Fig. 8a. The correlation of a single period cosine with a frequency equal to that of this dominant frequency yields the cross-correlation coefficient shown in Fig. 8b. Note that the signal looks similar to the negative of the original intensity, but the noise and any trend in the signal have been removed. The peak and valley locations of the correlation coefficient identified by the circular symbols correspond to the peak/valley locations of the original intensity signal. The correspondence between the peaks in valleys in Figs. 8a and 8b is excellent as indicated by the gray lines in the figures. The incidence angles at the peak/valley locations determined from the photogrammetry are shown in Fig. 8c, where a small but significant change in incidence angle is observed. Note that the incidence angles in other

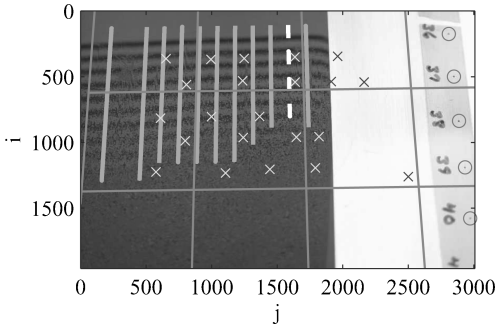

Fig. 7 Interferogram image from splitter plate downstream of the hump with analysis lines overlaid. The crosses represent reference point locations, the circles identify pressure tap locations, and the horizontal and vertical grid represent lines of constant x and z spaced 30 mm apart.

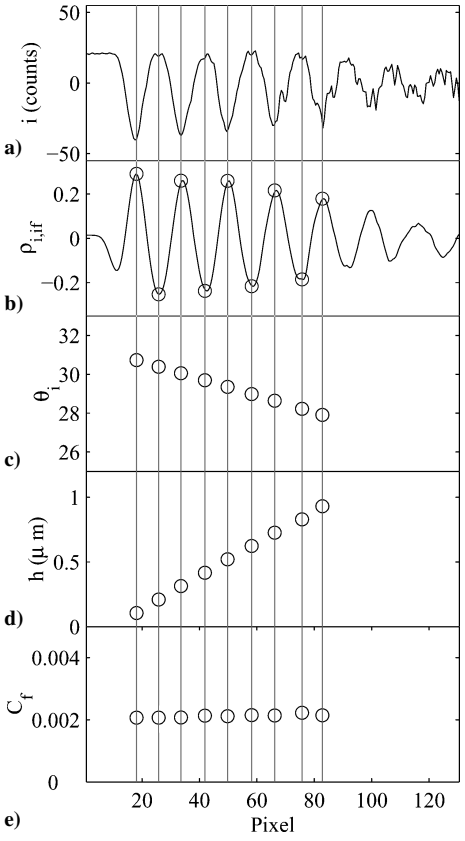

Fig. 8 Results from processing the analysis line shown as a white dotted line in Fig. 7: a) intensity with the mean removed, b) cross-correlation coefficient, c) incidence angle, d) oil height, and e) skin-friction coefficient.

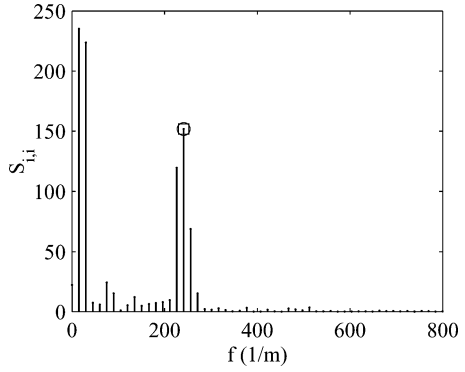

Fig. 9 Autospectral density of the intensity pattern extracted from the white dotted line in Fig. 7.

images acquired in this test varied much more significantly because of higher model curvature. Combining the incidence angle θ_i with the phase at the peak/valley locations allows for the determination of the oil-film height h using Eq. (4), and the result is shown in Fig. 8d. To complete the analysis, the skin friction is determined using h and the value of $\int_0^t (q/\mu)\,\mathrm{d}t$ with Eq. (2).

By repeating this process at several locations identified by the white lines in Fig. 7, a number of independent estimations of the skin friction are determined and are shown in Fig. 10a. Because this is a two-dimensional flow, all C_f values that fall within a given x range, regardless of the z location, can be averaged, and a precision uncertainty can be estimated. Such results are presented in Fig. 10b, where both the mean value and the precision uncertainty (95% confidence level) are shown.

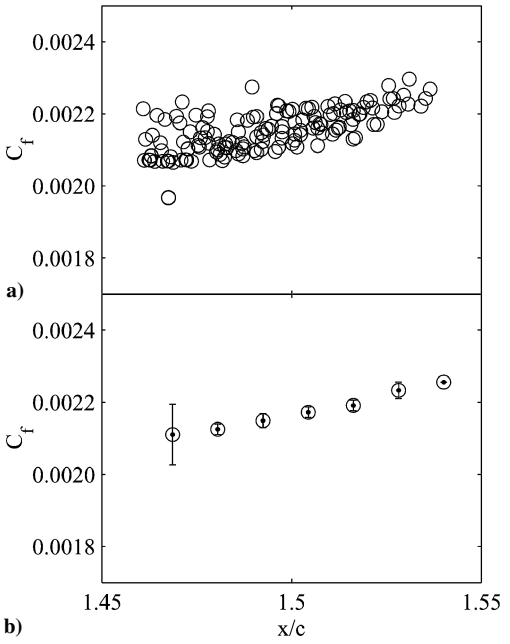

Fig. 10 Results from processing the analysis lines shown in Fig. 7: a) all analysis results and b) averaged results with precision uncertainty.

IV. Results

The analysis process just described has been applied to 25 different interferograms taken at different locations along the model. Several thousand individual C_f realizations have been averaged at many spatial locations along the model to determine estimates of the local skin friction. This section discusses these results and their use with other experimental data as well as their use in evaluating computational simulations.

A. Flow Visualization

In addition to the qualitative assessment of the surface flow provided by the oil-film interferograms in Fig. 2, oil-film interferometry was also used to determine the reattachment location downstream of separation. Oil was applied in discrete drops diagonally across a line that extended from the centerline in the negative z direction and corresponding to the previously measured reattachment x/c location (see Fig. 11). Oil films were generated using a method similar to that just described, with the exception that overlapping images were acquired by traversing the camera in the z direction along the span of the model. The images were then corrected for perspective and pieced together by matching corresponding fringes from the different images. A composite of the images resulting from this procedure is shown in Fig. 11. The oil-film method clearly can be used as a flow-visualization technique as well as yielding quantitative shear-stress data.

The composite of images shows that the reattachment line is essentially two-dimensional and, for most films, the downstream and upstream flow directions can be clearly identified. Although the reattachment line is essentially two-dimensional, there appears to be a crossflow component with the shear stress acting perpendicular to the reattachment line at some locations. Note, however, that the shear stress near reattachment is extremely low as can be seen by comparing the fringe spacing near the reattachment line ($x/c \approx 1.11$) with that at $x/c = 1.05$ and 1.15, where C_f is higher but still low (approximately -0.001 and 0.001, respectively). Note that, in regions of such low shear stress, the oil film is subject to other forces (e.g., pressure and gravity forces), which can dominate its behavior. For some of the oil drops applied on the reattachment line as well as those close to the end plates, the forces were not large enough to thin the oil sufficiently to generate fringes over the duration of the run. These results emphasize that, as with most flow visualization, it is important to know to what the visualization is sensitive.

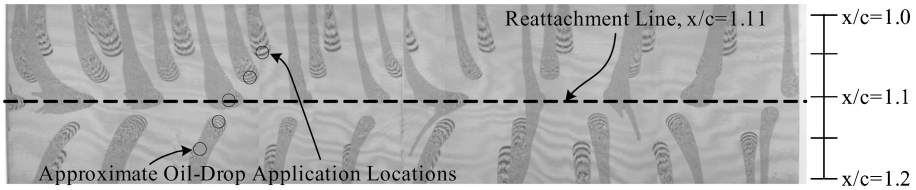

Fig. 11 Oil-film interferograms used to determine reattachment location.

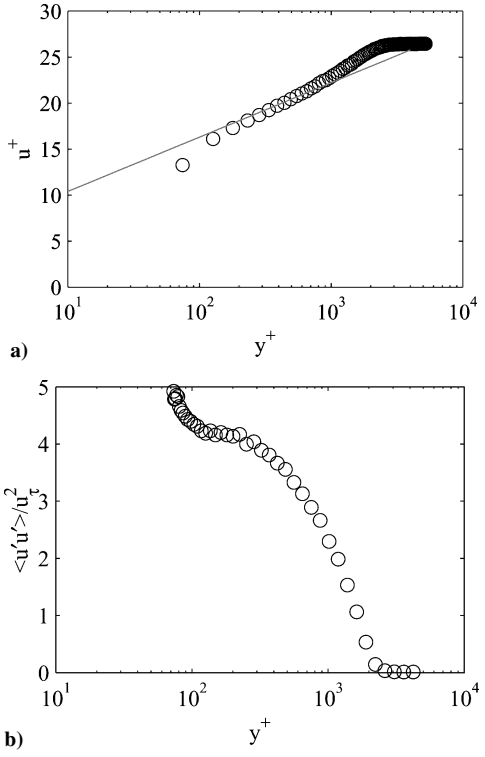

Fig. 12 Inflow velocity ($x/c \sim -2.14c$) with viscous scaling: a) streamwise mean velocity and b) streamwise normal Reynolds stress. The Reynolds number at this location based on momentum thickness is 6.8×10^3.

B. Skin-Friction Relation to Other Flowfield Measurements

One of the critical uses of skin friction is its use to determine the friction velocity u_τ for proper scaling of the boundary layer in viscous or wall units. An example of this is shown in Fig. 12a, where the mean inflow velocity u at $x/c = -2.14c$ determined using a flattened pitot tube has been plotted in wall units. Here the nondimensional velocity $u^+ = u/u_\tau$ has been shown as a function of the distance from the wall in viscous units $y^+ = yu_\tau/\nu$. In many instances, the friction velocity is determined by adjusting its value until this curve passes through the log-law result shown as a solid line in the figure. In this case, the friction velocity is determined from the shear stress measured using oil-film interferometry:

$$u_\tau = \sqrt{\tau_w/\rho} = \sqrt{C_f U_\infty^2/2} \tag{5}$$

Here, the velocity appears to deviate slightly from the expected behavior in the log region. However, this profile is taken near the leading edge of the splitter plate at a Reynolds number $Re_\theta = 6.8 \times 10^3$ where the profiles found using direct measurements of shear stress have been shown to be just approaching the standard log-law curve.[19] If this velocity had been forced to the standard log-law curve by varying u_τ and perhaps the wall origin, an incorrect result would be obtained.

The normal Reynolds stress $\langle u'u' \rangle$ measured using a hot wire at the same inflow location is shown in Fig. 12b with viscous scaling for both the velocity and distance from the wall. As just discussed, if a value for u_τ had been determined from a fit to the accepted equilibrium turbulent boundary-layer profile, the scaled values in this figure would contain significant errors. The normal Reynolds stress scaled using the measured skin-friction results in values that are not atypical of smooth wall turbulent boundary layers. Note that the viscous nondimensionalization and logarithmic scaling highlight the behavior of the fluctuating velocity near the wall. For example, the increase in $\langle u'u' \rangle/u_\tau^2$ when moving toward the wall from $y^+ = 20$ is broadened as compared to what it would look like (almost a vertical line) if this were plotted using linear scaling in outer coordinates (y/δ), which is another widely used method to plot these quantities. Here, measurements were not made at locations near enough to the wall to observe the expected drop off in the fluctuations as the wall is approached.

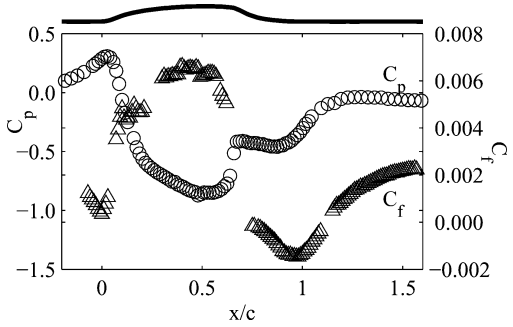

Fig. 13 Experimentally measured pressure and skin-friction coefficients.

The averaged C_f data are plotted in Fig. 13 along with the pressure coefficient $C_p = 2(P - P_\infty)/(\rho U_\infty^2)$. The quality of the skin-friction measurements in the separated region and the region downstream of reattachment is high. Note that the points near $x/c = 1.5$ have been obtained using 50-cS oil, whereas the remainder of the points in separation and reattachment have been acquired using 20-cS oil. The excellent overlap of these data occurs because the oils have been calibrated and the temperature on the plate has been carefully monitored. Note that no results have been obtained near reattachment and just downstream of separation because of the very low shear-stress levels in these regions. Unfortunately, the results near the top of the hump are not as good. This is attributed to poorer fringe quality that resulted from using oil with too low viscosity and artifacts in the fringes caused by surface imperfections in the Mylar. There are also gaps in the coverage on the forebody. However, the values near $x/c = 0$ are very consistent and clearly indicate the minimum C_f location just upstream of the hump.

The quantitative surface shear-stress results can now be used to provide a more exact characterization of the near-surface flow than can the flow visualization shown in Fig. 2. The flow approaches the hump, decelerates, and nearly separates just upstream of the hump. The flow then rapidly accelerates up over the hump, and a corresponding high shear stress is observed. As the flow passes over the top of the hump, it encounters an adverse pressure gradient, and the skin friction begins to drop. The flow separates near the slot and reattaches downstream at approximately $x/c = 1.115$. In between the separation and reattachment points, a large region of reverse flow exists near the surface. Near the reattachment point, the reverse flow accelerates upstream with a corresponding increase in negative C_f. At approximately 0.97 x/c, the reverse flow starts to decrease, and the shear stress drops as the flow continues upstream. Downstream

of reattachment, the flow accelerates as the boundary layer begins to recover. At $x/c = 1.57$, the skin friction is 0.0022 and continues to climb.

One of the advantages of making skin-friction measurements is that they provide information complementary to other surface and flowfield measurements. Such complementary results can be observed by considering the pressure coefficient and skin-friction distributions shown in Fig. 13. The details of the pressure measurements are discussed by Greenblatt et al.[2] Upstream of separation where the boundary layer is attached, the skin-friction and pressure coefficients behave in essentially opposite manners; when the skin friction increases, the pressure coefficient drops. This can be explained by the acceleration of the flow over the forward part of the model that causes the pressure to drop and the velocity to increase. Because of the velocity increase, the gradients at the wall increase causing the the skin friction to rise. However, the region behind separation shows a quite different result. The skin friction becomes negative downstream of separation in the region where reverse flow occurs. Downstream of separation, the shear stress decreases from zero to a minimum value (maximum negative value) at $x/c = 0.97$. In this same region, the pressure is essentially constant. Downstream of the minimum C_f location, the shear stress increases and reaches zero at the reattachment location and then slowly continues to rise as the boundary layer redevelops on the splitter plate. The pressure in this region also increases to a local maximum just downstream of reattachment and then begins a slow decrease. The different behavior of C_p and C_f occurs because the pressure in the separated region is largely sensitive to the flow above the wall, whereas the skin friction is sensitive to the flow directly above the wall. As a result, the skin friction provides a clearer indication of the the surface flow, but the two measurements are necessary to fully understand the surface forces (i.e., one measurement cannot be inferred from the other).

The skin-friction measurements have a similar impact when considered with flow-field measurements. Figure 14 shows the streamwise velocity downstream of separation measured using PIV. The PIV measurements, acquired using two-dimensional PIV, are discussed in detail by Greenblatt et al.[2] Skin-friction measurements from the same region are shown in the lower part of the figure. The skin-friction measurements can be used to clarify some of the flowfield results and vice versa. For example, the minimum skin friction occurs just upstream of where the hump transitions back to the flat surface and corresponds to the x location of the highest negative velocities in the recirculation zone. Because PIV measurements have not been obtained in the near-wall region, the skin-friction measurements help clarify surface flow features such as the reattachment location. Note that the zero-velocity contour does approach the wall in the vicinity of where the skin friction is predicted to pass through zero. The PIV measurements also confirm that, within the resolution of the measurement, no strong flow features exist just downstream of separation. This finding supports the absence of C_f measurements in this region because it should be very small and is expected to slowly approach zero as separation is approached from downstream. Although oil-film measurements might be possible in this region, they would require long test times and would have decreasing accuracy because the pressure gradient is relatively high and the shear stress is approaching zero. The downstream redevelopment of a boundary layer is supported by the increasing momentum near the wall and the rapid increase in shear stress. Note that the flow in the region downstream of reattachment is really the combination of a "wake-like" flow and a redeveloping boundary layer. This can be observed in slices through the velocity field taken at $x/c = 1.2$ and 1.3, just downstream of reattachment, that are shown in Fig. 15. The velocity profiles are shown both in an outer scaling (Fig. 15a) and, because direct measurements of skin friction are available, using inner scaling in Fig. 15b. The outer scaling reveals little except the flow is attached and the momentum is increasing with distance downstream. In contrast, the inner scaling suggests

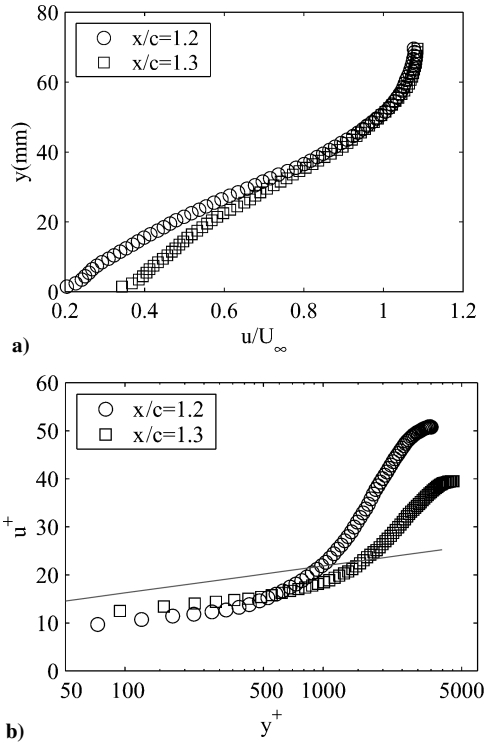

Fig. 15 Velocity profiles just downstream of reattachment shown in a) outer variables and b) viscous units.

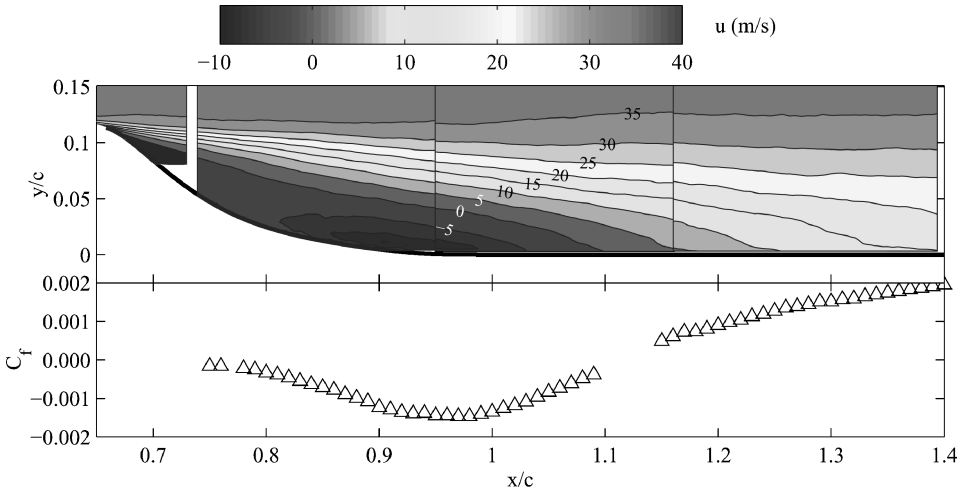

Fig. 14 Streamwise velocity downstream of separation measured with PIV. Also shown is the skin-friction distribution in the same range.

that, for the skin-friction levels in this region, there is relatively low momentum near the wall as compared to what would be expected for an equilibrium turbulent boundary layer, which accounts for the profiles falling below expected log-law values. Furthermore, the distance from the wall where the flow approaches a freestream velocity is very large: approaching 5000 wall units. From a near-wall perspective, the skin friction is high for this flow, which tends to cause y^+ to assume values that are larger than would be expected for a equilibrium turbulent boundary layer. It is clear that the velocity profile at $x/c = 1.3$ has increased momentum near the wall and a smaller wake as compared to the profile at $x/c = 1.2$. It would be expected that, if measurements were available farther downstream, the wake portion of the boundary layer would continue to diminish, and the momentum near the wall would continue to increase such that the boundary layer would recover toward an equilibrium turbulent boundary layer.

As is evident from the examples just given, shear stress measurements complement surface pressure and flow-field measurements obtained experimentally. However, another area where skin-friction measurements are valuable is for the assessment of computational simulations. Such comparisons are the primary reason these shear-stress measurements have been obtained and are the focus of the next section.

C. Comparison with Computational Results

The skin friction measured here provides an additional set of measurements for the validation of numerical simulations of the turbulent separated flow over the hump model. Although many simulations of the flow over the hump model have been carried out as part of the 2004 CFD Validation Workshop, only a small subset is considered here to demonstrate the usefulness of skin friction for evaluating numerical results and helping to pinpoint physical reasons for why the simulations succeed or fail. For a detailed description of the simulations discussed here, see Refs. 20–22. The computational results shown include two-dimensional simulations using the full unstructured Navier–Stokes (FUN2D) code[23] and structured CFL3D code.[24] Several turbulence models were used, and different grid densities were investigated. Computational flow analyses were conducted on the hump model for $M_\infty = 0.1$ at $Re_c = 9.36 \times 10^5$. For both flow solvers, the baseline cases analyzed were run nontime accurate and reached steady-state convergence.

1. Grids

The coordinates used to generate the grids were the two-dimensional, nondimensionalized theoretical model coordinates along with the tunnel geometry. The forward extent of these grids is longer than the actual splitter plate length used in the wind-tunnel experiment. This length was chosen to yield an inflow length such that the computed boundary-layer thickness approximately matched that of experimental data at $x/c = -2.14$. The grid height was identical to the actual distance between the splitter plate and the ceiling of the tunnel test section. Three different refinements of the unstructured grids were created and are referred to as the fine, medium, and coarse grids. The grid resolution at the surface was selected to capture viscous effects, while the ceiling used inviscid-type grid spacing. The medium structured grid contains four zones connected in a one-to-one fashion and had the same viscous-type wall spacing for the splitter plate and inviscid-type wall spacing for the ceiling. Grid-convergence studies were conducted, and examples of the effects of grids and turbulence models can be seen in Refs. 20 and 21.

2. Boundary Conditions

The boundary conditions on the hump model, the internal cavity walls, and the tunnel floor corresponded to no slip between the fluid and the solid boundary at their interface, with a constant temperature wall that was set to the adiabatic wall temperature. The tunnel ceiling was treated as an inviscid surface as was the actuator boundary at the bottom of the hump cavity. To obtain the boundary conditions at the tunnel inlet, the flow was assumed to be both inviscid and isentropic in this region so that quantities for the computation of the flux along the inflow boundary were obtained from two locally one-dimensional Riemann invariants. The Riemann invariants were considered constant along characteristics defined normal to the inflow boundary. At the downstream boundary, a backpressure of 0.99947 of the reference pressure was specified in order to approximate the upstream conditions at the tunnel inlet, and all other quantities were extrapolated from the interior of the domain.

3. Turbulence Models

The solutions from the CFL3D code shown here used three different turbulence models: the Spalart–Allmaras model,[25] the two-equation shear-stress transport model of Menter (SST),[26] and an explicit algebraic stress model (EASM-ko) in k–ω form.[27] The first two models are both linear eddy-viscosity models that make use of the Boussinesq eddy-viscosity hypothesis, whereas the EASM-ko is a nonlinear model. The solutions for FUN2D shown here used only the Spalart–Allmaras model.[25]

4. Numerical/Experimental Results Comparison

Skin-friction distributions predicted by simulations performed using the two solvers just described are shown in Fig. 16. The computations appear to capture the skin-friction distribution as the flow approaches and accelerates over the top of the hump. The deceleration upstream of the hump in all of the computations appears to be excessive. All of the simulations approach $C_f = 0$, and some drop slightly below, whereas the experimental measurements show

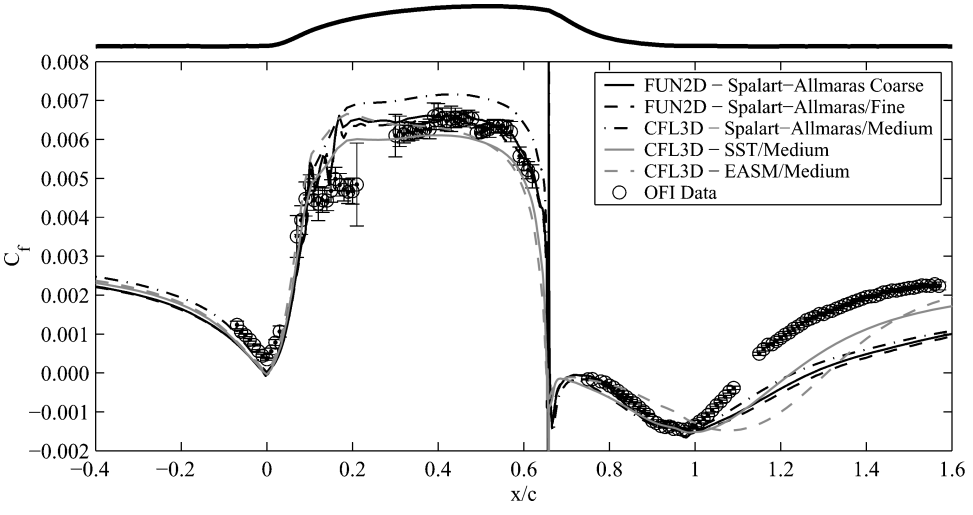

Fig. 16 Averaged experimental skin-friction measurements on the hump model with several CFD predictions shown. The model profile is shown above the figure for clarity.

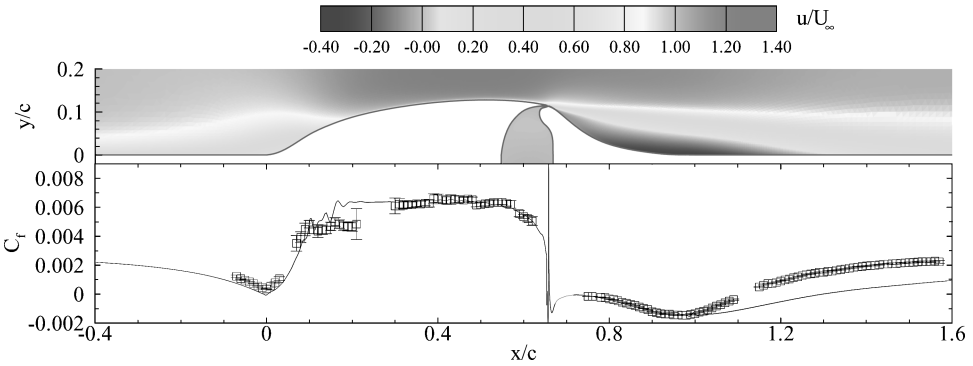

Fig. 17 Streamwise velocity above the hump model simulated with FUN2D using the finest grid and the Spalart–Allmaras turbulence model. Also shown is the skin-friction distribution from the same simulation and the experimentally measured skin friction.

a higher finite shear stress. The acceleration over the ramp and corresponding increase in wall shear stress are captured by all of the models, but the plateau level on the top of the hump varies between 0.006 (CFL3D with SST turbulence model) and 0.007 (CFL3D with Spalart–Allmaras turbulence model). It is disappointing that the scatter in the measured values is so high here that the measured C_f values also bracket these levels. Therefore, no comment on which simulation is able to capture the peak skin friction more accurately can be made. As the flow encounters an adverse pressure gradient just upstream of separation, all of the simulations respond with a corresponding drop in skin friction although the skin-friction levels remain scattered.

In the separation and reattachment region, the CFD calculations have trouble capturing the reattachment point, and thus the C_f levels in the separated region upstream of reattachment and the recovery region downstream of reattachment are poorly predicted. Also, the rate at which the skin friction grows in the recovery region (representative of the reacceleration of the flow) is missed by all CFD calculations using the Spalart–Allmaras turbulence model. The SST turbulence model appears to capture the recovery rate, whereas the EASM model overpredicts it. The models do appear to approach the experimental results in the upstream portion of the separated region, but this is probably a result of the conditions enforced by separation (i.e., $C_f = 0$). That said, the simulations show a rapid increase of negative skin friction just downstream of separation. This feature is discussed further next.

As with the experimental results, more understanding of the flow can be had if the flowfield and surface quantities are compared. Figure 17 shows the nondimensional streamwise velocity in the hump region computed using the FUN2D code. Shown beneath the flowfield are the skin friction from the same computation as well as the experimentally determined, C_f. All of the features of the computed skin friction just discussed, C_f too low at the beginning of the forebody, reattachment at a location too far downstream, and the high negative C_f just downstream of separation, are related to features in the flow above the surface. Although the location of reattachment is poorly predicted by the computation, the other two features are more subtle: In these cases, the computed flowfield can be used to assess the differences between the computed and measured values. For example, computational streamlines near the leading edge of the hump ($x/c = 0$) indicate a small separation in this region in contrast to the measurements. Although the shear stress is small in this region, it is not so low as to believe the oil-film measurements are incorrect. The differences in the measured and computed shear stress are small, but there are important local differences between a separating flow and one that remains attached. Another region where the computed and experimental skin-friction measurements show small differences is in the region just downstream of the slot. In this region, the computed and measured skin-friction values agree until $x/c \sim 1.0$. However, just downstream of separation, the computations are showing a large negative skin friction in a region where no measurements exist. When the skin friction in this region was first observed, we suspected that a smaller secondary separation existed

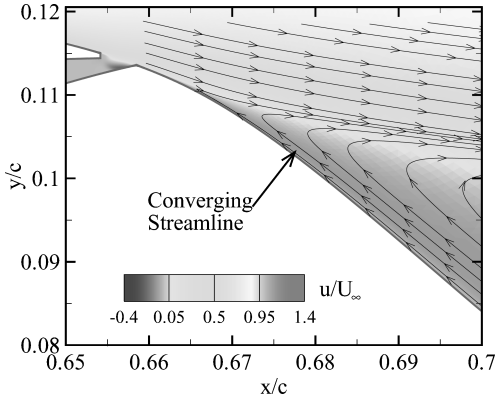

Fig. 18 Close-up of the streamwise velocity and streamlines near the slot exit. This result is from a simulation using FUN2D with the fine grid and the Spalart–Allmaras turbulence model.

because the skin friction approached zero and then became negative again. However, no secondary separation region was evident in the PIV measurements (see Fig. 14). Close inspection of the computed flowfield in this region indicates that something else is responsible (at least in this simulation). The streamlines shown in Fig. 18 show that no secondary separation exists. Instead, it is the convergence of the streamlines in the reverse flow as separation is approached, which causes the flow to accelerate in the upstream direction. This is particularly evident in the streamline nearest to the surface. This acceleration causes the shear stress to become increasingly negative, even though separation is being approached. Although the computation is consistent, the results in this region should be considered with caution because the entire separated region is suspect as a result of the poor prediction of reattachment. Thus, the agreement in the upstream portion of separation should be considered fortuitous, and the high negative shear stress just downstream of separation should be suspect. Future measurements in the region just downstream of separation could identify what structure (if any) exists in that region that is too small to see with PIV.

From this discussion, the value of skin-friction measurements for assessing computational methods is clear. Coupled with pressure and flowfield measurements, a fairly complete picture of the flow is obtained. Another observation is that the computational results can be used to guide measurements (i.e., what locations are most important to investigate), but some caution must be used as the simulations might miss important features in certain portions of the flow.

V. Conclusions

The skin-friction distribution on a wall-mounted hump model, including regions of reverse flow and areas with high-wall shear-stress gradients, has been successfully measured using oil-film interferometry. Comparison with experimental velocity and pressure

measurements show the value of the skin-friction measurements in obtaining a more complete picture of the flow physics. The comparison of the experimentally measured skin friction with values derived from computations carried out using the FUN2D and CFL3D solvers also underscores its power as a metric for wall-bounded flow simulations.

In addition to addressing these primary goals of the experiment, this study demonstrates that high accuracy measurements are possible on complex models if the measurements are carried out with attention to the details of the technique. In particular, proper calibration of the oil is a well known, and necessary requirement and proper photogrammetry methods should be applied to ensure accurate knowledge of the surface being imaged and the viewing angle. Because techniques such as oil-film interferometry are available, low uncertainty should be demanded of future studies that include skin-friction measurements for validation purposes. Unfortunately, oil-film interferometry is only applicable for mean skin-friction values, and flows with large temperature gradients will continue to be a challenge.

The comparisons of the experimentally measured skin friction with the several computational results highlight the use of such measurements for detecting regions where turbulence models are performing poorly in the near-wall region. For example, the experimental results indicate that the flow stays attached at the front of the model, whereas the simulations all indicate a small separated zone. Comparisons using skin friction with it high sensitivity to near-wall behavior of the flow are absolutely critical for evaluating turbulence models in flows such as that studied here, particularly as these turbulence models grow more sophisticated.

Acknowledgments

The first author acknowledges partial support from NASA Langley Research Center under a contract to Wyoming Instrumentation Development. This work was performed while the third author held a National Research Council NASA Langley Research Center Associateship. The authors thank Tianshu Liu of NASA Langley Research Center for his help with the photogrammetry issues and Steve Wilkinson of NASA Langley Research Center for his help with image issues. The authors also thank Chris Rumsey of NASA Langley Research Center, who provided a description of the CFL3D code and the simulations discussed in this paper.

References

[1]Seifert, A., and Pack, L. G., "Active Flow Separation Control on Wall-Mounted Hump at High Reynolds Numbers," *AIAA Journal*, Vol. 40, No. 7, 2002, pp. 1363–1372.

[2]Greenblatt, D., Paschal, K., Schaeffler, N., Washburn, A., and Yao, C., "Separation Control over a Wall-Mounted Hump: A CFD Validation Test Case," AIAA Paper 2004-2219, June 2004.

[3]Bradshaw, P., Cantwell, B. J., Ferziger, J. H., Kline, S. J., Rubesin, M., and Horstmann, C. C., "Experimental Data Needs for Computational Fluid Dynamics," *Proceedings of the 1980-81-AFOSR-HTTM-Stanford Conference on Complex Turbulent Flows*, edited by S. J. Kline, B. J. Cantwell, and G. M. Lilley, Stanford Univ., Stanford, CA, 1981, pp. 23–35.

[4]Tanner, L. H., and Blows, L. G., "A Study of the Motion of Oil Films on Surfaces in Air Flow, with Application to the Measurement of Skin Friction," *Journal of Physics E: Scientific Instrumentation*, Vol. 9, No. 3, 1976, pp. 194–202.

[5]Squire, L. C., "The Motion of a Thin Oil Sheet Under the Boundary Layer on a Body," *Flow Visualization in Wind Tunnels Using Indicators*, AGARDograph 70, edited by R. L. Maltby, 1962, pp. 7–23.

[6]Monson, D. J., Mateer, G. G., and Menter, F. R., "Boundary-Layer Transition and Global Skin Friction Measurement with an Oil-Fringe Imaging Technique," Society of Automotive Engineers, Paper 932550, Sept. 1993.

[7]Zilliac, G., "Further Developments of the Fringe-Imaging Skin Friction Technique," NASA TM 110425, Dec. 1996.

[8]Garrison, T. J., and Ackman, M., "Development of a Global Interferometer Skin-Friction Meter," *AIAA Journal*, Vol. 36, No. 1, 1998, pp. 62–68.

[9]Naughton, J. W., and Brown, J. L., "Surface Interferometric Skin-Friction Measurement Technique," AIAA Paper 96-2183, June 1996.

[10]Driver, D. M., "Application of Oil-Film Interferometry Skin-Friction Measurement to Large Wind Tunnels," *Experiments in Fluids*, Vol. 34, No. 5, 2003, pp. 717–725.

[11]Naughton, J. W., and Sheplak, M., "Modern Developments in Shear Stress Measurement," *Progress in Aerospace Sciences*, Vol. 38, No. 6–7, 2002, pp. 515–570.

[12]Brown, J. L., and Naughton, J. W., "The Thin Oil Film Equation," NASA TM 1999-208767, March 1999.

[13]Davy, C., Alvi, F. S., and Naughton, J. W., "Surface Flow Measurements of Micro-Supersonic Impinging Jets," AIAA Paper 2002-3196, June 2002.

[14]Naughton, J. W., Robinson, J., and Durgesh, V., "Oil-Film Interferometry Measurement of Skin Friction—Analysis Summary and Description of MATLAB Program," *ICIASF 2003 Record, 20th International Congress on Instrumentation in Aerospace Simulation Facilities*, Inst. of Electrical and Electronics Engineers, IEEE 03CH37501, 2003, pp. 169–178.

[15]Decker, R. K., Naughton, J. W., and Jafari, F., "Automatic Fringe Detection for Oil Film Interferometric Skin Friction Measurement," *Proceedings of the 9th International Symposium on Flow Visualization* [CD ROM], edited by I. Grant and G. M. Carlomagno, Paper 367, 2000, pp. 367-1–367-8.

[16]Cattafesta, L. N., III, and Moore, J. G., "Review and Application of Non-Topographic Photogrammetry to Quantitative Flow Visualization," AIAA Paper 96-2180, June 1996.

[17]Liu, T., Cattafesta, L. N., III, Radetsky, R. H., and Burner, A. W., "Photogrammetry Applied to Wind-Tunnel Testing," *AIAA Journal*, Vol. 38, No. 6, 2000, pp. 964–971.

[18]Naughton, J. W., and Brown, J. L., "Uncertainty Analysis for Oil-Film Interferometry Skin-Friction Measurement Techniques," American Society of Mechanical Engineers, Paper FEDSM97-3475, June 1997.

[19]Karlsson, R. I., "Studies of Skin Friction in Turbulent Boundary Layers on Smooth and Rough Walls," Ph.D. Dissertation, Applied Thermo and Fluid Dynamics, Chalmers Tekniska Högskola, Göteborg, Sweden, Sept. 1980.

[20]Rumsey, C. L., "Case 3: RANS and URANS Application with CFL3D," *CFD Validation of Synthetic Jets and Turbulent Separation Contro*, Vol. 1: Contributed Papers, 2004, pp. 3.8.1–3.8.5, http://cfdval2004.larc.nasa.gov/index.html.

[21]Viken, S. A., "Case 3: Two-Dimensional Flow Control Analysis on the Hump Model," *CFD Validation of Synthetic Jets and Turbulent Separation Control*, Vol. 1, Contributed Papers, 2004, pp. 3.10.1–3.10.5, http://cfdval2004.larc.nasa.gov/index.html.

[22]Rumsey, C. L., Gatski, T. B., Sellers, W. L., Vatsa, V. N., and Viken, S. A., "Summary of the 2004 CFD Validation Workshop on Synthetic Jets and Turbulent Separation Control," AIAA Paper 2004-2217, June–July 2004.

[23]Anderson, W. K., and Bonhaus, D. L., "An Implicit Upwind Algorithm for Computing Turbulent Flows on Unstructured Grids," *Computers and Fluids*, Vol. 23, No. 1, 1994, pp. 1–21.

[24]Krist, S. L., Biedron, R. T., and Rumsey, C. L., *CFL3D User's Manual*, ver. 5.0, NASA TM-1998-208444, June 1998.

[25]Spalart, P. R., and Allmaras, S. R., "A One-Equation Turbulence Model for Aerodynamic Flows," AIAA Paper 92-0439, Jan. 1992.

[26]Menter, F. R., "Two-Equation Eddy-Viscosity Turbulence Models for Engineering Applications," *AIAA Journal*, Vol. 32, No. 8, 1994, pp. 1598–1605.

[27]Rumsey, C. L., and Gatski, T. B., "Summary of EASM Turbulence Models in CFL3D with Validation Test Cases," NASA TM-2003-212431, June 2003.

T. Beutner
Guest Editor